Directed-Energy Laser-Thermal Propulsion for Rapid Transit Missions in the Solar System

Zhuo Fan Bao*, Emmanuel Duplay†, Alp Tanriover‡ and Andrew Higgins§
McGill University, Montreal, QC, H3A 0C3

Laser thermal propulsion as a potential interplanetary travel method is investigated in light of recent developments in fiber-optic lasers that can be phase-locked to act as a single optical element. This study considers the power output and mass of a laser-thermal propelled spacecraft in order to determine a specific mass (α) of the propulsion system. The study on power output examines the heated plasma behaviour inside the heating chamber through numerical simulations of laser-supported combustion (LSC) waves. A preliminary spacecraft design is performed to estimate the mass of a laser thermal rocket capable of rapid transit missions within the solar system. Synthesizing the different aspects of the analysis, the study concludes that an α of $\approx$ 0.01 kg/kW is achievable, and laser thermal propulsion could be a candidate for future high Δv interplanetary missions.

I. Introduction

The emergence of inexpensive fiber-optic-based lasers that can be phased-locked together to act as a single optical element of very large dimension has the potential to be a disruptive technology for deep-space propulsion. By using a modular architecture of phase-locked laser amplifiers, a scalable system is able to deliver directed energy at different fluxes to spacecraft for a wide variety of missions and payload classes. For instance, direct photon pressure applied to a lightsail could propel spacecraft to speeds far greater than achievable with existing or envisioned propulsion technologies: A large (10 km) laser array focusing an energy flux of 100 GW/m^2 onto a one-meter lightsail could accelerate an ultra-low mass "wafersat" to greater than 20% the speed of light in an acceleration time of a few minutes, paving the way for true interstellar flight [1].

Alternatively, more modest laser arrays can provide power to electric propulsion thrusters with high-efficiency solar cells tuned to the laser frequency at fluxes on the order of 10 kW/m^2 (i.e., ten "suns"). In a 2018 NIAC study [2], Brophy et al. discussed the preliminary design of this propulsion architecture, targeting a maximum velocity of more than 40 AU per year given a kilometer-scale 100 MW laser array and a 40,000 s specific impulse lithium-ion thruster. This system is well matched for interstellar precursor missions—long duration (several years) transits to the outer edge of the solar system, targeting the interstellar medium or the solar gravitational focus (550 AU). Ultra-high specific impulse is less well suited to fast interplanetary missions, such as Earth-to-Mars transit in a month, due to the inherent low-thrust associated with electric propulsion systems. Furthermore, kilometer-scale arrays represent a significant technological leap that is unlikely to be the first demonstration of directed energy propulsion.

Laser thermal propulsion, a high thrust propulsion method with specific impulse intermediate between chemical and electric propulsion, is another potential approach to the use of directed energy. Deployable lightweight reflectors can focus the laser beam into a heating chamber that heats a working fluid, likely hydrogen, to ionization temperatures, which is then expanded through a conventional nozzle. The elimination of onboard oxidizer and power, the potential ability to operate at very high power and thrust levels, and the simple and lightweight hardware onboard the spacecraft may make laser thermal propulsion well suited for rapid interplanetary travel [3, 4]. The high laser power enables the acceleration phase of the mission to occur in near-Earth space, such that a much smaller phased array is required (order of 10 m in size), potentially making this approach a near-term application of the phased array technology.

Laser thermal propulsion was extensively studied in the 1970s and 1980s, where CO_2 lasers operating at 10.6 μm were usually assumed as the laser source [5, 6]. The use of longer wavelength and meter-scale optics would limit the application to either earth-to-orbit launch for small vehicles (due to power limitations) or orbit raising from low earth orbit (LEO). The distance a laser of optical diameter d can deliver energy to a target of size D is of the order of

*Undergraduate Research Assistant, Department of Mechanical Engineering, 817 Sherbrooke St. W., Student Member AIAA.
†Undergraduate Research Assistant, Department of Mechanical Engineering, 817 Sherbrooke St. W.
‡Undergraduate Research Assistant, Department of Mechanical Engineering, 817 Sherbrooke St. W.
§Professor, Department of Mechanical Engineering, 817 Sherbrooke St. W., Senior Member AIAA.

$\frac{dD}{\lambda}$; a 1-m-diameter laser operating at 10 μm would only be able to focus energy onto a 10-m-diameter receiver to a distance on the order of 1000 km (i.e., LEO). The present study considers the implications of revisiting the laser thermal propulsion concept using 1-μm-wavelength fiber-optic lasers operating as a dense phased array with dimensions of order 10 m in diameter, and thus able to deliver energy to 100,000 km. The earlier research on laser thermal propulsion provides a basis that informs the present study.

Laser thermal propulsion operates in two different regimes—repetitively pulsed and continuous wave. Laser thermal propulsion directly deposits energy into the propellant, which is then exhausted through a thrust conversion system [7]. Repetitively pulsed (RP) laser propulsion uses a pulsed laser of very great fluence to ablate the propellant and to superheat it to form plasma [7, 8]. This method requires the pulse frequency to be synchronized with the propellant and a laser capable of producing very high fluence [8]. The present study is, in contrast, focused on the propulsion applications of continuous wave (CW) lasers, as this approach is well-suited to the phased array of fiber-based lasers approach.

Continuous wave (CW) laser propulsion heats the propellant and sustains a steady-state plasma. For hydrogen, CW laser propulsion can operate at laser intensities above the maintenance threshold ($2.6 \times 10^4 - 29.5 \times 10^4$ W/cm^2) as predicted numerically by Jackson and Nielsen [9] and experimentally by Conrad et al. [5], but faces absorption zone instabilities that can hinder plasma generation [4, 8].

The present study is a revisit of the concept of laser thermal propulsion in light of the developments in fiber-optic lasers. It will focus on CW laser propulsion for rapid transit missions in the solar system.

II. Thrust Optimization

Fundamental considerations of thrust and specific impulse can help to match propulsion technologies and missions. CW laser thermal rockets exhaust at a constant mass flow rate. The total change of spacecraft velocity, ΔV, is given by the rocket equation

$$\Delta V = I_{\mathrm{sp}}\, g_0\, \ln \frac{m_{\mathrm{i}}}{m_{\mathrm{f}}} \text{ (Ref. [10, 11])}, \tag{1}$$

where I_{sp} is the specific impulse, g_0 is the gravitational constant, and $\frac{m_{\mathrm{i}}}{m_{\mathrm{f}}}$ is the initial (entire vehicle) to final (entire vehicle without the propellant) mass ratio of the spacecraft.

In order to perform several of the missions described in the Introduction, a ΔV of around 30 km/s is necessary. To achieve ΔVs on that order of magnitude, mass ratio $\frac{m_{\mathrm{i}}}{m_{\mathrm{f}}}$ and I_{sp} would need to be maximized. Due to physical limitations of a rocket not being able to be entirely made out of propellant, the mass ratio optimization is limited despite the advantage gained by eliminating oxidizer and a power source on board the rocket. Thus, the only parameter in the rocket equation left is I_{sp}, the efficiency of the propellant. A higher I_{sp} would translate to higher ΔVs possible for a rocket with the same mass ratio. I_{sp} depends on the exhaust gas temperature (T_{e}) and molecular weight (MW) of the propellant in a square root fashion

$$I_{\mathrm{sp}} \sim \sqrt{\frac{T_{\mathrm{e}}}{\mathrm{MW}}} \text{ (Ref. [4])} \tag{2}$$

Currently, the best chemical hydrogen-oxygen rockets have an I_{sp} of about 450 s because the reaction is limited to temperatures of around 3500 K and creates products of around 12 kg/kmol molecular weight [4]. On the other hand, owing to high chamber temperature and low propellant molecular weight, laser thermal propulsion rockets can theoretically achieve a specific impulse beyond 1000 s, making it a very desirable option for rapid interplanetary transits.

I_{sp}, although important, is not the only parameter that should be considered in optimization. Especially for short duration missions such as a 30-45 days transit-to-Mars flyby, time limitations must also be factored into consideration. For power-constrained spacecraft, there exists a trade-off between thrust and I_{sp} as shown in the following equation:

$$P_{\mathrm{r}} = \frac{F\, I_{\mathrm{sp}}\, g_0}{2\, \eta} \text{ (Ref. [4])}, \tag{3}$$

where P_{r} is power input to the rocket, F is thrust, and η is thrust conversion efficiency.

As seen in Fig. 1, the trade-off for high I_{sp} is low thrust, which translates to longer acceleration and laser beam operation times. For example, ion electric propulsion features impressive specific impulse on the order of several thousands of seconds at the expense of lower thrust, and therefore would take almost 10 days to reach the necessary ΔV.

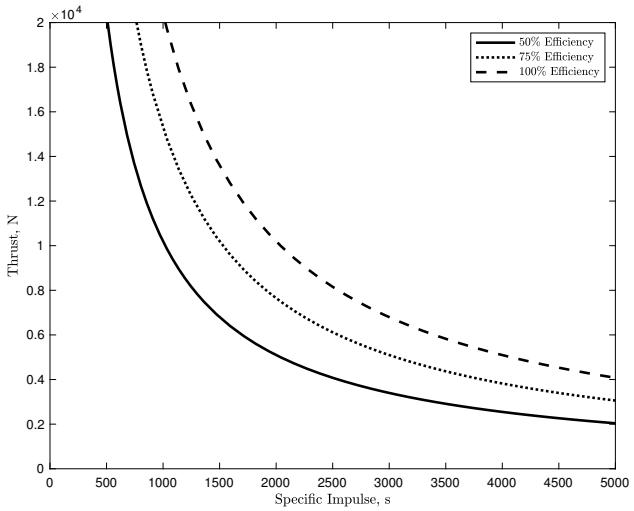

Fig. 1 Power-limited rocket thrust and specific impulse trade-off.

While this regime is valuable for long term missions where a 10-day acceleration time is negligible, higher I_{sp} is not suitable for rapid interplanetary missions due to time and technical limitations:

- Shorter acceleration time implies laser near field limit can be closer to launch site, which implies the vehicle can be accelerated using a small laser array (on the order of 10 m) and act as a proof of concept mission.
- Longer acceleration times associated with laser-electric propulsion also imply that several laser arrays would need to be built world-wide (similar to the Deep Space Network) or the laser array might need to be constructed in space in order to continuously beam to the spacecraft over long periods of time.
- Shorter acceleration times per mission allows for greater mission frequency. E.g., several missions could be launched by a single laser array during a launch opportunity of planetary alignment.

Stuhlinger derived an optimization method that maximizes payload mass and determines the I_{sp} as a function of propellant burn time

$$v_{ch} = \sqrt{\frac{2\,\eta\,t_b}{\alpha}} \text{ (Ref. [12])}, \tag{4}$$

where η is the thrust conversion efficiency, t_b is the propellant burn time, α is the specific power and v_{ch} is the Stuhlinger velocity, which is the velocity the exhaust would achieve by converting all the available energy to thrust at a constant rate within the burn time.

Figure 2 shows that as burn time shortens; specific impulse must decrease to provide enough acceleration. It also illustrates the necessity of an α of around 0.01 kg/kW to accelerate to the necessary ΔV in a constrained burn time.

III. Laser Sustained Plasma

The heating chamber, the crux of a laser thermal rocket, converts the delivered laser energy into enthalpy for the nozzle to expand. Laser energy is deposited into a plasma, which serves as an energy conversion system. To ensure the least amount of energy is lost, it is crucial to understand the absorption and emission mechanisms happening inside the chamber. In this section, the physics of the laser deposition process is reviewed.

A. Absorption Mechanisms

Laser gas continuous absorption mechanisms involve both bound-free (photoionization) and free-free (inverse bremsstrahlung) energy transitions of the gas. Photoionization is the process through which gas releases ions by absorbing photons and is a highly wavelength-dependent process that does not occur frequently. On the contrary, inverse bremsstrahlung absorbs radiation in a non-resonant fashion using its free electrons. Thus, absorption in the plasma is dominated by free-free transitions because 1 μm laser light is not resonant with hydrogen [13].

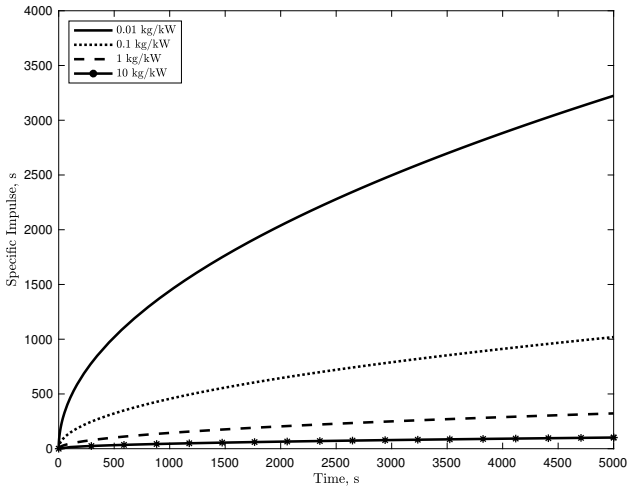

Fig. 2 Stuhlinger optimized specific impulse in terms of burn time.

B. Transient State

Lasers can generate or sustain plasmas in various different ways that depend on the intensity, spot size, and mode of operation of the laser beam and on the propellant gas conditions. High energy RP lasers can directly cause breakdown within the gas by ablating the propellant similar to an explosion, but CW lasers can only provide enough energy to sustain the plasma in a continuous fashion and would need a secondary source to initialize plasma breakdown.

After breakdown, a plasma can propagate to the surrounding cold gas in three different ways: laser-supported combustion (LSC), laser-supported detonation (LSD), and laser-supported radiation (LSR) absorption waves. The propagation method can heavily influence the final steady-state plasma.

The LSC wave appears in low intensity sustained plasmas because it only requires maintenance threshold laser intensity to stabilize. The ambient gas is heated by passing through a precursor shock and by the radiation of the already formed plasma. LSD wave is a regime, situated in between LSC and LSR, where the precursor shock itself is able to heat the gas to initiate absorption. LSD waves operate at higher temperatures and laser intensities than LSC waves: the transition happens between 5-20 MW/cm^2 and seems to be largely wavelength independent. At higher laser intensities, the plasma radiation is strong enough to heat the ambient gas to initiate laser absorption. This is referred to as the LSR wave regime where the plasma temperature is on the order of 100,000 K and requires nearly a GW/cm^2 of laser intensity to be sustained [13].

To accomplish the various missions discussed in the Introduction, LSC waves are the most optimal regime to operate the rocket in because they require a lower intensity to maintain and do not radiate excessively outwards. The ideal plasma should be as large as possible without excessive thermal loads to the walls of the heating chamber. LSD and LSR waves both reach too high temperatures, thus increasing its radiation and require a laser flux that would overly constrain plasma size.

C. Steady State

The constant pressure expanding LSC wave will eventually reach steady-state as it expands along the laser beam to a point where laser absorption and heat loss reach a balance. One- [14, 15] and two-dimensional [16] models of the LSC wave have been developed in the past, but all assumed a CO_2 10.6 μm laser as the directed energy source. This study replicates the results from the previous papers for steady state LSC waves but applied to 1-μm fiber optic lasers.

The temperature profile of the LSC wave can be solved using the conservation laws. To preserve the one-dimensional assumption, mass flux must be constant:

$$\rho\, v = \rho_0\, v_0 = \text{constant}, \tag{5}$$

where ρ is the mass density, v is the fluid velocity and zero subscript refers to initial conditions. Due to the assumption that pressure is constant, the momentum equation is eliminated from consideration. Finally, the conservation of energy equation is a balance of energy exchanges between the plasma and its surrounding:

$$\rho_0 \, v_0 \, c_p \, \frac{\mathrm{d}T}{\mathrm{d}x} = \frac{\mathrm{d}}{\mathrm{d}x}(\lambda_\mathrm{c} \, \frac{\mathrm{d}T}{\mathrm{d}x}) + k_\mathrm{L} \, I - \phi, \tag{6}$$

where c_p is the heat capacity, T is the temperature of the plasma, x is the distance along the laser beam, λ_c is the thermal conductivity, k_L is the absorption coefficient for laser radiation, I is the laser beam intensity, and ϕ is the radiation loss in W/m^3.

In order to solve for the temperature profile of the LSC wave, the solution is decoupled into two distinct regions: post-absorption and absorption regions [15]. The post-absorption region (from 0 to ∞) is the region at the back of the plasma where the plasma has cooled back down and cannot absorb laser energy anymore (laser intensity not necessarily zero). The laser absorption region (from 0 to $-\infty$) is the region where the plasma experiences heating from the laser and is solved from the back ($x = 0$) to the front of the plasma ($x = -\infty$).

1. Post-Absorption

To obtain the temperature profile of the plasma, solve for the BVP:

$$\rho_0 \, v_0 \, c_p \, \frac{\mathrm{d}T}{\mathrm{d}x} = \frac{\mathrm{d}}{\mathrm{d}x}(\lambda_\mathrm{c} \, \frac{\mathrm{d}T}{\mathrm{d}x}) - \phi \tag{7}$$

with boundary conditions:

$$T(0) = 8500 \text{ K} \tag{8a}$$

$$T(\infty) = 6000 \text{ K} \tag{8b}$$

ρ_0 and u_0 are chosen based on initial conditions. The values of c_p, λ_c, and ϕ will be discussed in the appendix.

There are many ways to solve the BVP, such as the shooting method. One possible method is to perform a change of variables with relaxation [17]:

$$\xi = \frac{1}{1 + x} \tag{9}$$

2. Absorption

For the absorption region (from 0 to $-\infty$), the temperature profile of the plasma is solved from the back ($x = 0$) to the front ($x = -\infty$) of the plasma because it is difficult to initialize the heating process when solving the ODE from the front.

The ODE is broken into an autonomous system of three first-order equations:

$$\frac{\mathrm{d}T}{\mathrm{d}x} = -\frac{q}{\lambda_\mathrm{c}} \tag{10a}$$

$$\frac{\mathrm{d}q}{\mathrm{d}x} = \frac{\rho_0 \, v_0 \, c_p}{\lambda_\mathrm{c}} \, q + k_\mathrm{L} \, I - \phi \tag{10b}$$

$$\frac{\mathrm{d}I}{\mathrm{d}x} = -k_\mathrm{L} \, I, \tag{10c}$$

where q is the thermal flux. The value of k_L is discussed in the appendix.

The initial conditions of the ODE ($x = 0$) are computed from the solution of the BVP solved above at $x = 0$:

$$T_\text{initial} = T_\text{BVP}(0) \tag{11a}$$

$$q_\text{initial} = -\lambda_\mathrm{c} \, \frac{\mathrm{d}T}{\mathrm{d}x}_\text{BVP}(0) \tag{11b}$$

To preserve continuity, the initial temperature of the ODE is taken as is from the BVP. The initial thermal flux of the ODE is calculated from the slope of the temperature at $x = 0$. Finally, the initial laser beam intensity (I_0) is guessed and iterated upon until the ODE shoots to the temperature desired.

Optimal operation of the heating chamber by increasing flow velocity and limiting plasma size can allow for near 100% laser beam absorption [5].

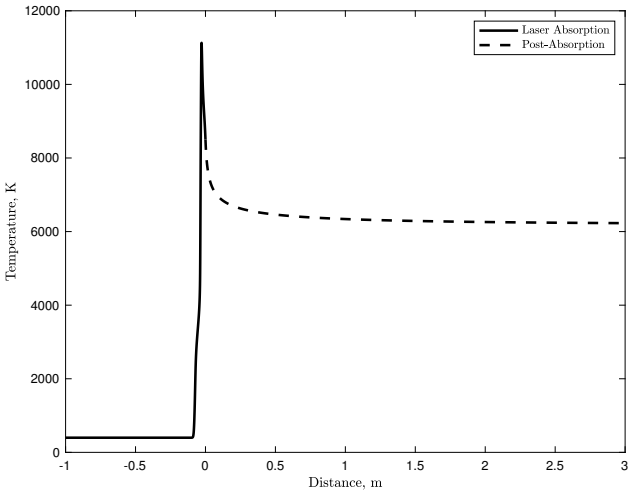

Fig. 3 Plasma temperature profile.

IV. Radiation Loss

For emission, the plasma loses a significant portion of heat through radiation loss in free-bound (recombination), free-free (bremsstrahlung), and bound-bound (line radiation) transitions [18].

As the hydrogen heats up, radiation becomes an important energy transfer mechanism. While it is beyond the scope of this paper to deal with all aspects of the radiation loss, radiation exchange between the hot plasma and the cold propellant gas flowing around it is crucial to the LSC model because radiation is the most important loss mechanism and is the limiting factor to the peak plasma temperature. It is also necessary to characterize heat reabsorption by the cold propellant and heat loss to the heating chamber walls. The radiation exchange happening inside the plasma is omitted from the LSC model above because it is considered negligible compared to the flux of the laser beam.

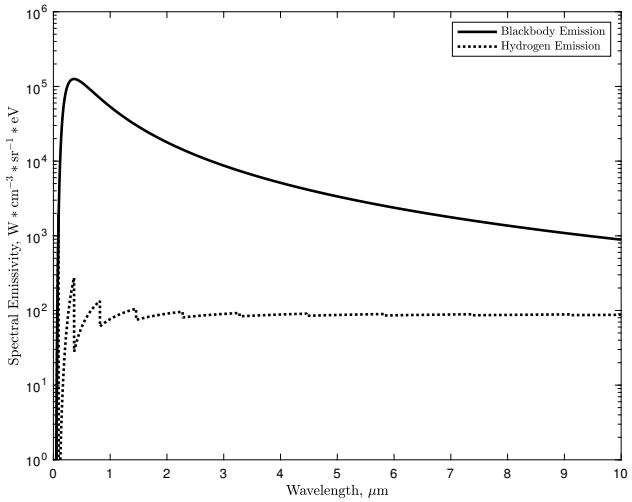

Fig. 4 Comparison between blackbody radiation and hydrogen emission at 14,000 K.

Interestingly, as seen in Fig. 4, due to effects such as broadening and bremsstrahlung, high temperature hydrogen emits continuously along the spectrum with peak line radiations several orders of magnitude below blackbody radiation [19].

Previous work on LSC wave radiation losses have shown that optimal coupling of the laser can decrease radiation loss from the plasma to 35% [13]. Due to cold hydrogen being practically invisible to all radiation, emission of this proportion can be dangerous for the chamber walls and can lead to massive loss of enthalpy and exhaust velocity. Seeding the hydrogen with gases more resonant to one-micron laser at cold temperatures or using pre-ionized hydrogen have both been considered as methods to preserve enthalpy [13] and will require further investigation. Shoji et al. [20],

in their investigation of heat transfer mechanisms inside a laser thermal heating chamber, have concluded that seeding can reduce power loss to the wall down to 5% by taking advantage of convective cooling by the flowing hydrogen and of radiative cooling by the seeded particles.

V. Specific Impulse

For laser-heating chambers exceeding 5000 K, the hydrogen is expected to be fully dissociated, and for temperatures approaching 20,000 K, the hydrogen will be fully ionized. As both dissociated and ionized hydrogen is monatomic, this feature enables a simple estimate of exhaust velocity assuming the chemical composition remains fixed (i.e., frozen flow) through the expansion process. From conservation of energy

$$h_0 = h + \frac{v^2}{2} \tag{12}$$

For a monatomic gas of fixed composition, $h = c_p T = \frac{5}{2}\frac{R_u}{\mathrm{MW}}T$, so the exhaust velocity is given by

$$V_{\mathrm{exit}_{\mathrm{frozen}}} = \sqrt{2(h_0 - h_{\mathrm{exit}})} = \sqrt{5\frac{R_u}{\mathrm{MW}}\left(T_0 - T_{\mathrm{exit}}\right)} \tag{13}$$

This value of exhaust velocity is plotted in Fig. 5, normalized by g_0, assuming complete expansion of products to vacuum, as a function of the heating chamber temperature.

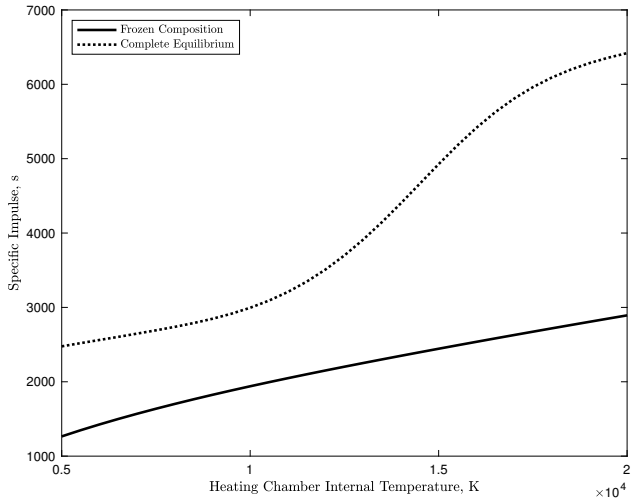

Fig. 5 Specific impulse based on expansion from chamber temperature.

In practice, as the hydrogen expands and cools, recombination to atomic and then molecular hydrogen will release additional energy into the flow. This is accounted for by including the enthalpy of formation as follows

$$h_0 = h^0_{\mathrm{f_H}} + \alpha_0\, h^0_{\mathrm{f_{H+}}} + c_{p\ \mathrm{diatomic}}(T_0 - T_{\mathrm{ref}}) = h^0_{\mathrm{f_{H_2}}} + c_{p\ \mathrm{monatomic}}(T_{\mathrm{exit}} - T_{\mathrm{ref}}) + \frac{v^2_{\mathrm{exit}}}{2} \tag{14}$$

where α is the ionization fraction given by Eq. 28 or Eq. 29 (Ref. [19]) and complete recombination has been assumed in the exhaust products. The enthalpy of formation terms h^0_{f} takes into account the energy released in electron recombination and the forming of chemical bonds; $h^0_{\mathrm{f_{H_2}}} = 0$ by definition. Solving for exhaust velocity

$$V_{\mathrm{exit}_{\mathrm{equilibrium}}} = \sqrt{2(h^0_{\mathrm{f_H}} + \alpha_0\, h^0_{\mathrm{f_{H+}}}) + 5\frac{R_u}{\mathrm{MW}}\left(T_0 - T_{\mathrm{ref}}\right) - 7\frac{R_u}{\mathrm{MW}}\left(T_{\mathrm{exit}} - T_{\mathrm{ref}}\right)} \tag{15}$$

which is also plotted in Fig. 5 for case of complete expansion to vacuum.

The two solutions plotted in Fig. 5 represent the specific impulse for the two cases considered here (frozen and equilibrium flow) and should bound the actual performance of a laser thermal propulsion system, minus additional losses.

VI. Mission Design

Based on our understanding of the physics reviewed in the previous sections, we will present a notional design for a laser thermal propulsion spacecraft, carrying a 1000 kg payload (equivalent to Mars Exploration Rover missions) to a Mars intercept within 30 to 45 days. We assume the system is driven by a ground-based, 1 μm, 100 MW phased array laser with a 10 m aperture, and that the laser is ideally focused on the spacecraft's reflector. The propulsion system is split into three major subsystems: the propellant feed system, the laser reflector and the heating chamber. Each subsystem's mass is estimated in order to determine the overall specific power (α) parameter of a laser thermal rocket.

A. Heating Chamber

Taking into consideration technical limitations, a two-port heating chamber design [21] was considered based on both its expected mechanical and thermal loads. An Inconel X-750 [22] cylindrical container 1 m long and 0.25 m in radius is considered. Assuming a best-case scenario of 5 MW of heat transmitted to the chamber walls and a chamber pressure of 100 kPa, both a hoop stress calculation and a steady-state heat transfer analysis is performed to determine the optimal wall thickness. The former suggests a minimum wall thickness of 0.12 mm. Furthermore, the chamber is designed with regenerative cooling in mind—pre-heating liquid hydrogen before it is injected in the chamber. Conventional chemical rocket walls deal with radiation levels above a magnitude of MWs, thus using regenerative cooling for this design is very reasonable.

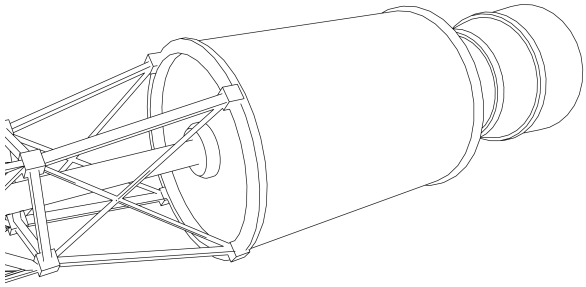

Fig. 6 Heating chamber concept drawing.

Before solving the heat transfer problem, a thermodynamic analysis is performed to determine the temperature of the liquid hydrogen at the exit of the cooling jacket. Considering a constant pressure (300 kPa) heat addition process for a mass flow rate of 1 kg/s yields an approximate exit temperature of 372 K, according to data from [23].

To determine the inner wall temperature, the heat transfer problem is set up as a simple conduction problem [24]:

$$q = \kappa \frac{T_{\text{inner}} - T_{\text{outer}}}{t_{\text{w}}} \tag{16}$$

Where κ is the thermal conductivity of Inconel, T_{outer}, the outer wall temperature, is assumed to be equal to the coolant hydrogen's exit temperature of 372 K, q is calculated as though 5 MW were evenly distributed on the curved surface of the cylinder, and t_{w}, the wall thickness, is derived from hoop stress. Solving for T_{inner} suggests an internal wall temperature of 388 K.

Such chamber dimensions result in a mass of 1.9 kg, leaving more than enough leeway mass for nozzle, cooling system and extra structural mass.

B. Feed System and Propellant Tank

The proposed feed system consists of a monopropellant tank which in turn reduces the overall feed system weight compared to current bipropellant designs. Furthermore, LH_2 is selected as the propellant due to its low molecular weight. However, just like any other cryogenic fuel, LH_2 storage is challenging as it needs to be stored aboard at temperatures of 20 K and a pressure of 300 kPa [25].

For preliminary design considerations, 2195-T8 aluminum-lithium alloy is selected for its flight heritage as the Space Shuttle's super-lightweight cryogenic tank material [25]. The propellant tank is spherical by design to have

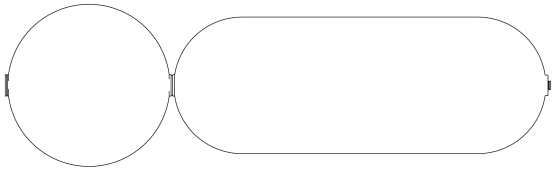

Fig. 7 Helium (spherical) and hydrogen (cylindrical) tanks concept drawing.

the highest expulsion efficiency. Given that the chamber operates at a relatively low pressure (100 kPa), we select a pressure-fed solution instead of a heavier, more elaborate turbopump-driven system. We assume a one-hour burn with a mass flow rate of 1 kg/s, thus requiring 3.6 tons of propellant.

Table 1 Assumptions and properties of the material.

Properties	Values
Factor of Safety	1.5
$F_{yield,Al-2195-T8}$	560 MPa
Propellant Density	70.99 kg/m^3
Burn Duration	3600 s
$\dot{m}$	1 kg/s
Mass Propellant	3600 kg
Propellant Volume	50.7 m^3

Using the method presented in [26], we approximate the overall mass of the feed system by considering its three major components: the main fuel tank, the pressurizing gas tank and the pressurizing gas mass. The evaluation incorporates safety and ullage factors for a realistic mass estimate but does not take into account piping and insulation materials. Helium is chosen as a pressurizing gas for its low molecular weight—it will be seen in a later section that this is the same gas used for the laser reflector, which hints at a possible dual-use gas tank, further reducing overall system mass. Finally, we assume both the fuel tank and the gas tank are made of the same material, 2195-T8 aluminum-lithium alloy [27].

Table 2 Feed system mass using 2195-T8 aluminum-lithium alloy.

Component	Mass (kg)
LH_2 Tank	192.5
Helium Tank	337.6
Helium Gas	78.55
Total	**648.7**

It is possible to further reduce the mass of the propellant and pressurizing gas tanks using Composite Over-wrapped Pressure Vessels (COPVs). Currently, COPV's are being heavily researched for cryogenic propellant tanks as they are capable of providing high burst pressures for a low mass. There exist many different composite combinations (S-Glass/Epoxy, Carbon/Epoxy, etc..), manufacturing methods and fiber-to-resin ratios. To preserve high tensile strength and accommodate cryogenic temperatures, a Kevlar-49/Epoxy composite is chosen. The proposed propellant tank

consists of titanium metallic liners with an overwrap of Kevlar-49 fiber in an epoxy matrix [28]. To obtain an estimate of the new tank mass, we will assume that most of the weight is provided by Kevlar-49/Epoxy composite. Furthermore, it is assumed that the fiber to resin ratio is 60% Kevlar-49 and 40%, as is standard in the aerospace industry. Additionally, it is assumed that the manufacturing of the composites is ideal, that is, there are no air or dust particles within the volume ratio. Using the same tank parameters calculated from the 2195-T8 aluminum-lithium alloy and knowing the densities of Kevlar-49 (1.47 g/cm^3) and epoxy (1.25 g/cm^3) the propellant tank and feed system masses are recalculated and shown in Table 3.

Table 3 Feed system mass using Kevlar/epoxy COPV.

Component	Mass (kg)
LH_2 COPV Tank	36.99
Helium COPV Tank	70.58
Helium Gas	78.55
Total	**185.1**

C. Mirror & Optics

The spacecraft's optics must capture the incoming laser beam (assumed to be parallel rays) and focus it onto the heating chamber, which can be performed with a parabolic reflector.

To facilitate manufacturing, in-orbit assembly, and deployment, and to greatly minimize the propulsion system's mass (thus reducing the α), we propose the use of inflatable optics instead of solid mirrors. Significant work has been performed in this domain for applications in astronomy, telecommunications, and solar-thermal propulsion: for instance, a 2 by 3-meter inflatable reflector prototype (Torus Supported Concentrator, TSC-6) was tested by the Marshall Spaceflight Center, for potential use with a solar orbital transfer vehicle [29].

We propose an identical, albeit scaled-up, design for our spacecraft. Such inflatable systems use modest internal pressures ranging from 1 to 100 Pa [29, 30], and thus would require very light auxiliary components, i.e., support structures and pressurization tanks. To approximate the overall mass of the optics system, we start by creating a rough model of the reflector in SolidWorks to determine its internal volume and surface area. The reflector is parametrized as a paraboloid with a 6 m focal length, a projected circular face 10 m in diameter, with a tensioning torus on its perimeter. This design has an internal volume of 97.8 m^3 and a surface area of 272.46 m^2. We choose helium as a pressurizing gas for its low molecular weight and extremely low boiling point.

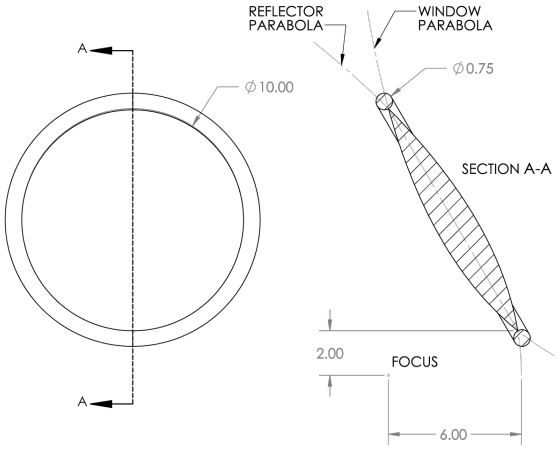

Fig. 8 Inflatable reflector concept drawing.

From this, we determine the gas mass from the ideal gas law, at an internal pressure of 100 Pa and assuming a temperature of 300 K:

$$m = \frac{P\,V}{R_g\,T} = 0.0157 \text{ kg} \tag{17}$$

This agrees with data provided by the NIST [23].

The empty reflector mass is simply estimated by multiplying its surface area with polyimide's density and a typical thickness value for commercial polyimide films of 0.05 mm [31], yielding a mass of 19.3 kg. Finally, we consider the mass of the helium tank, assumed spherical, used to store the pressurizing gas before deployment. We first derive the tank's radius from its volume, calculated from a desired storage state of 100 kPa at 200 K. Using 6061 aluminum (density of 2700 kg/m^{-3} and tensile yield strength of 276 MPa [32]) as wall material with a safety factor of 1.5, the minimum wall thickness can be calculated from hoop stress:

$$t_w = \frac{P\,r}{2\,\sigma} = 0.069 \text{ mm} \tag{18}$$

The empty tank mass can then be computed:

$$m = \rho_{\text{Al–6061}}\,\frac{4\,\pi}{3}\,((r + t_w)^3 - r^3) = 0.144 \text{ kg} \tag{19}$$

This gives a total system mass of 19.5 kg, excluding minor structural components, inflatable support struts, insulation material and pressure feed systems. Varying parameters such as the gas temperature in the reflector and the tank yields a total mass ranging from 20 to 50 kg. As stated earlier, the helium storage tank could be foregone by tapping into the already existing pressurizing tank of the feed system. This inflatable reflector would be offset from the spacecraft's longitudinal axis such that the rest of the propulsion system would not interfere with the laser's path. Given the low mass of the reflector compared to the other modules of the system, the impact of this off-axis configuration on the center of mass is either negligible or easily compensated.

D. Preliminary Design

Based on our understanding and analysis of laser thermal propulsion, we can propose a preliminary design of the rocket. The most crucial components such as the propellant tank, reflector and heating chamber were included. The total estimated propulsion system mass is 670 kg using conventional aluminum fuel tanks, or 206.5 kg using Kevlar/Epoxy composites. Note that this fails to account for the nozzle, thrust chamber cooling jacket, miscellaneous structural components, piping and other auxiliary modules' masses. This nevertheless is quite promising for achieving an α of 0.01 kg/kW, as the above mass figures fall well below the 1000 kg limit for a 100 MW power input rocket.

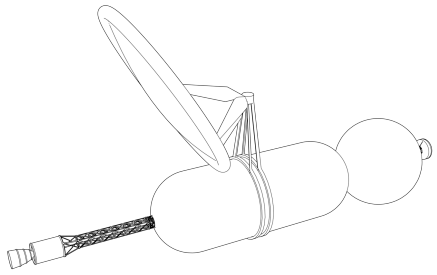

Fig. 9 Conceptual spacecraft.

VII. Conclusion

In this paper, we have reviewed the most crucial aspects of a CW laser thermal propulsion spacecraft and updated prior laser thermal research from the 1970s and 1980s considering 1-μm fiber-optic-lasers. We have also determined an α value for our proposed spacecraft design. To do so, we provided an overview of the need for I_{sp} and thrust for short duration missions, solved the temperature profile of the plasma, and considered absorption and radiation effects inside

the heating chamber. We have also calculated the mass of the most important components of the spacecraft based on our preliminary design. The α value for laser thermal propulsion shows promise, and laser thermal propulsion could be a solution for rapid transit interplanetary travel.

Appendix

This appendix documents the methods used to obtain specific heat, absorption length, thermal conductivity and radiation loss of hydrogen at different temperatures. In order to properly account for the dissociation and ionization effects of hydrogen, a switch was incorporated into the model [14]:

$$T^* = 2000 \log_{10}(P \text{ (in atm)}) + 7000 \tag{20}$$

where if $T \geq T^*$, then it is assumed all hydrogen has fully dissociated. On the other hand, if $T < T^*$, then it is assumed no ionization effects take place.

A. Dissociation vs. Ionization

The ionization and dissociation ratios are calculated in different ways depending on the temperature based on Kemp's study [19].

$$\theta_\mathrm{I} = 158000 \text{ K} \tag{21}$$

$$\theta_\mathrm{r} = 87.62 \text{ K} \tag{22}$$

$$\theta_\mathrm{v} = 5983 \text{ K} \tag{23}$$

$$\theta_\mathrm{D} = 52000 \text{ K} \tag{24}$$

$$S_1 = \sum_{n=1}^{17} n^2 \exp\left(\frac{\theta_\mathrm{I}}{Tn^2}\right) \tag{25}$$

For $T \geq T^*$:

$$\beta = 1 \tag{26}$$

$$f_I = \left(\frac{2\pi m_\mathrm{E} k}{{h_\mathrm{P}}^2}\right)^{3/2} \frac{kT^{5/2}}{S_1} \tag{27}$$

$$\alpha = \left(1 + \frac{P \text{ (in Pa)}}{f_\mathrm{I}}\right)^{-1/2} \tag{28}$$

For $T < T^*$:

$$\alpha = 0 \tag{29}$$

$$f_D = \left(\frac{\pi m_\mathrm{A} k}{{h_\mathrm{P}}^2}\right)^{3/2} 2k\theta_\mathrm{r} T^{3/2} (1 - \exp(-\theta_\mathrm{v}/T)) \exp(-\theta_\mathrm{D}/T) \tag{30}$$

$$\beta = \left(1 + \frac{P \text{ (in Pa)}}{f_\mathrm{D}}\right)^{-1/2} \tag{31}$$

where α is the ionization ratio, β is the dissociation ratio, θs are state temperatures of hydrogen, f_I and f_D are function definitions. m_E is the electron mass and m_A is the hydrogen atom mass:

$$m_\mathrm{E} = 9.109 * 10^{-31} \text{ kg} \tag{32a}$$

$$m_\mathrm{A} = 1.673 * 10^{-27} \text{ kg} \tag{32b}$$

k is the Boltzmann constant and h_P is the Planck constant:

$$k = 1.38064852 * 10^{-23} \ \frac{\mathrm{J}}{\mathrm{K}} \tag{33a}$$

$$h_\mathrm{P} = 6.62607015 * 10^{-34} \text{ J} * \text{s} \tag{33b}$$

B. Specific Heat

The specific heat of the system is obtained by taking the cubic spline of Patch's tables on thermodynamic properties for 1 atm [33].

C. Thermal Conductivity

The thermal conductivity is interpolated using a cubic spline from Grier's tables. For $T \geq T^*$, Grier's tables on ionizing hydrogen [34] is interpolated, and for $T < T^*$, Grier's tables on dissociating hydrogen [35] is used instead.

D. Absorption Length

Absorption length (in m^{-1}) is modeled based on the following equations [19]:

$$k_{\mathrm{LEI}} = 8.7 \times 10^8 \; \alpha^2 \; \beta^2 \; \frac{\rho_0^2}{\sqrt{T}} \; (\exp\left(13570/T\right) - 1) \tag{34a}$$

$$Q_{\mathrm{EN}} = \frac{2.96 \times 10^{-45} T}{1 - \exp \frac{-h_{\mathrm{P}}\; c}{\lambda \; k \; T}} \; \left(\frac{\theta_{\mathrm{I}} \; k \; \lambda}{h_{\mathrm{P}} \; T \; c}\right)^2 \; \sqrt{\theta_{\mathrm{I}}/T} \tag{34b}$$

$$k_{\mathrm{LEN}} = 4 \; Q_{\mathrm{EN}} \; \alpha \; (1 - \alpha) \; \rho_0 \; \sqrt{T} \; (1 - \exp\left(\frac{-h_{\mathrm{P}} \; c}{\lambda \; k \; T}\right))/10^{-4} \tag{34c}$$

$$k_{\mathrm{L}} = k_{\mathrm{LEI}} + k_{\mathrm{LEN}} \tag{34d}$$

where c is the speed of light, Q_{EN} is the absorption cross-section, k_{LEI} is the absorption coefficient for electron-ion absorption and k_{LEN} is the absorption length for electron-neutral absorption. k_{L} is the total absorption coefficient.

E. Radiation Loss

The radiation loss model is given by [19]:

$$\phi = 5.1 \times 10^{18} \; \times 2 \; \left(\frac{T}{\theta_{\mathrm{I}}} + 0.4\right) \; \frac{T}{\theta_{\mathrm{I}}} \; \beta \; (1 - \alpha) \; \frac{\rho_0}{S_1} \tag{35}$$

Acknowledgments

The work described in this paper is supported by Natural Sciences and Engineering Research Council of Canada (NSERC) and the McGill Summer Undergraduate Research in Engineering program. The authors thank Philip Lubin, Carl Knowlen, Mélanie Tétreault-Friend, and Pascal Hubert for providing valuable insight and feedback.

References

[1] Lubin, P., "A Roadmap to Interstellar Flight," *Journal of the British Interplanetary Society*, Vol. 69, 2016, pp. 40–72.

[2] Brophy, J., Polk, J., Alkalai, L., Nesmith, B., Grandidier, J., and Lubin, P., "A Breakthrough Propulsion Architecture for Interstellar Precursor Missions: Phase I Final Report," Tech. rep., NASA, 2018.

[3] Kare, J. T., "Pulsed laser thermal propulsion for interstellar precursor missions," *AIP Conference Proceedings*, Vol. 504, AIP, 2000, pp. 1278–1284.

[4] Krier, H., and Glumb, R., "Concepts and status of laser-supported rocket propulsion," *Journal of Spacecraft and Rockets*, Vol. 21, No. 1, 1984, pp. 70–79.

[5] Conrad, R., Pyles, C., Roy, E., and Mangum, D., "Laser-Supported Combustion Wave Ignition in Hydrogen." Tech. rep., ARMY MISSILE COMMAND REDSTONE ARSENAL AL DIRECTED ENERGY DIRECTORATE, 1979.

[6] Welle, R., Keefer, D., and Peters, C., "Laser-sustained plasmas in forced argon convective flow. I-Experimental studies," *AIAA Journal*, Vol. 25, No. 8, 1987, pp. 1093–1099.

[7] Cook, J. R., "Laser Propulsion—Is it another myth or a real potential?" *AIP conference proceedings*, Vol. 997, AIP, 2008, pp. 109–118.

[8] Nebolsine, P. E., and Pirri, A. N., "Laser propulsion: the early years," *AIP Conference Proceedings*, Vol. 664, AIP, 2003, pp. 11–21.

[9] Jackson, J., and Nielsen, P., "Role of radiative transport in the propagation of laser supported combustion waves," *AIAA Journal*, Vol. 12, No. 11, 1974, pp. 1498–1501.

[10] Mallinckrodt, J., "F does not equal d (mv)/dt," *The Physics Teacher*, Vol. 48, No. 6, 2010, pp. 360–360.

[11] Benson, T., "Ideal Rocket Equation," , 2014. URL https://www.grc.nasa.gov/WWW/K-12/rocket/rktpow.html, [Online; accessed 01-July-2019].

[12] "Mission Analysis for Electric Propulsion," , 2015.

[13] Radziemski, L. J., and Cremers, D. A., *Laser-induced plasmas and applications*, Marcel Dekker Inc., 1989.

[14] Kemp, N. H., and Root, R. G., "Analytical study of laser-supported combustion waves in hydrogen," *Journal of Energy*, Vol. 3, No. 1, 1979, pp. 40–49.

[15] Keefer, D., Peters, C., and Crowder, H., "A re-examination of the laser-supported combustion wave," *AIAA Journal*, Vol. 23, No. 8, 1985, pp. 1208–1212.

[16] Jeng, S.-M., Keefer, D. R., Welle, R., and Peters, C. E., "Laser-sustained plasmas in forced convective argon flow. II-Comparison of numerical model with experiment," *AIAA Journal*, Vol. 25, No. 9, 1987, pp. 1224–1230.

[17] Patankar, S., *Numerical heat transfer and fluid flow*, CRC press, 2018.

[18] Ohji, T., and Eagar, T. W., "Infrared radiation from an arc plasma and its application to plasma diagnostics," *Plasma chemistry and plasma processing*, Vol. 12, No. 4, 1992, pp. 403–419.

[19] Kemp, N., Root, R., Wu, P., Caledonia, G., and Pirri, A., "Laser-Heated Rocket Studies," Tech. rep., Physical Sciences Inc Andover, MA, 1976.

[20] Shoji, J., and Larson, V., "Performance and heat transfer characteristics of the laser-heated rocket-A future space transportation system," *12th International Electric Propulsion Conference*, 1976, p. 1044.

[21] Legner, H., and Douglas-Hamilton, D., "CW laser propulsion," *Journal of Energy*, Vol. 2, No. 2, 1978, pp. 85–94.

[22] "Inconel Alloy X-750," , 2004. URL http://www.specialmetals.com/assets/smc/documents/alloys/inconel/inconel-alloy-x-750.pdf, [Online; accessed 12-July-2019].

[23] Lemmon, E., "Thermophysical Properties of Fluid Systems, NIST chemistry WebBook, NIST standard reference database number 69," *NIST Chemistry WebBook*, 2005.

[24] Sutton, G. P., and Biblarz, O., *Rocket propulsion elements*, John Wiley & Sons, 2010.

[25] "Super Lightweight External Tank," , 2005. URL https://www.nasa.gov/sites/default/files/113020main_shuttle_lightweight.pdf, [Online; accessed 01-July-2019].

[26] Solda', N., and Lentini, D., "Opportunities for a liquid rocket feed system based on electric pumps," *Journal of propulsion and power*, Vol. 24, No. 6, 2008, pp. 1340–1346.

[27] "2195 (2195-T8) Aluminum," , 2018. URL https://www.makeitfrom.com/material-properties/2195-2195-T8-Aluminum, [Online; accessed 01-July-2019].

[28] Kezirian, M., Johnson, K., and Phoenix, S., "Composite overwrapped pressure vessels (COPV): Flight rationale for the Space Shuttle Program," *AIAA SPACE 2011 Conference & Exposition*, 2011, p. 7363.

[29] Engberg, R., Lassiter, J., and McGee, J., "Modal survey test of the SOTV 2x3 meter off-axis inflatable concentrator," *41st Structures, Structural Dynamics, and Materials Conference and Exhibit*, 2000, p. 1639.

[30] Patiño-Jiménez, F., Nahmad-Molinari, Y., Moreno-Oliva, V. I., Los Santos-García, D., Santiago-Alvarado, A., et al., "Construction and optical testing of inflatable membrane mirror using structured light technique," *International Journal of Photoenergy*, Vol. 2015, 2015.

[31] "Polyimide Metallized Film Material Information," , 2019. URL http://www.goodfellow.com/A/Polyimide-Metallized-Film.html, [Online; accessed 01-July-2019].

[32] "Aluminum 6061-T6; 6061-T651," , 2001. URL http://asm.matweb.com/search/SpecificMaterial.asp?bassnum=MA6061T6, [Online; accessed 01-July-2019].

[33] Patch, R., "Thermodynamic properties and theoretical rocket performance of hydrogen to 100,000 K and 1.01325 x 10 to the 8th power N/sq m," Tech. rep., NASA, 1971.

[34] Grier, N. T., "Calculation of transport properties of ionizing atomic Hydrogen," Tech. rep., NASA, 1966.

[35] Grier, N. T., "Calculation of transport properties and heat transfer parameters of dissociating hydrogen," Tech. rep., NASA, 1962.